

# CSCI 596 Final project

## Simulating and visualizing the discharging process in $\text{Li}_{2x}\text{Mn}_2\text{O}_4$

Delin Zhang (USCID: 7081442424)

Aerospace and Mechanical Engineering, University of Southern California, Los Angeles, CA 90089, USA

### Abstract

This study investigates lamellar microstructure formation in Spinel  $\text{Li}_{2x}\text{Mn}_2\text{O}_4$  (LMO) electrodes during lithium intercalation. Experimental evidence affirms the emergence of distinctive textures, such as lamellar microstructures, during particle discharging. Utilizing a multi-scale thermomechanical continuum phase field model implemented in C++ within MOOSE and executed on USC CARC, our simulations offer insights into microstructural evolution during lithium intercalation in LMO. Comparisons between our modeling predictions and in-situ bright field imaging of LMO microstructures demonstrate qualitative agreement, validating the model's ability to capture the interplay between Li-diffusion and lattice deformations. This modeling framework enhances our understanding of lithium intercalation dynamics and provides a computational tool for predicting and designing microstructural evolution in electrode materials.

## Background

Spinel  $\text{Li}_{2x}\text{Mn}_2\text{O}_4$  (LMO) is an economical and environmentally friendly material capable of accommodating lithium up to  $x = 1$  per chemical unit while maintaining the fundamental arrangement of manganese-oxygen octahedrons. In the  $0 < x < 0.5$  range, the crystal structure remains cubic, and only the lattice expands with increasing  $x$ . When the lithium content exceeds  $x = 0.5$ , the previously tetrahedrally coordinated lithium migrates to octahedral sites, while the oxygen-manganese arrangement remains unaltered but is accompanied by a notable Jahn-Teller distortion. This leads to the emergence of a two-phase region involving  $\text{LiMn}_2\text{O}_4$  and  $\text{Li}_2\text{Mn}_2\text{O}_4$ , concurrently giving rise to lamellar microstructures.

Validation of these phenomena is provided by experimental findings from Erichsen et al.,[1] which affirm that, during the discharging process, LMO particles not only undergo volumetric expansion but also generate distinctive textures, exemplified by lamellar microstructures (refer to Fig. 1).

The primary objective of this project is to provide a mechanistic explanation for the formation of lamellar microstructures within the framework of LMO. C++ codes are implemented using Multiphysics Object-Oriented Simulation Environment (MOOSE), simulations are executed on USC CARC, and results are visualized utilizing Paraview.

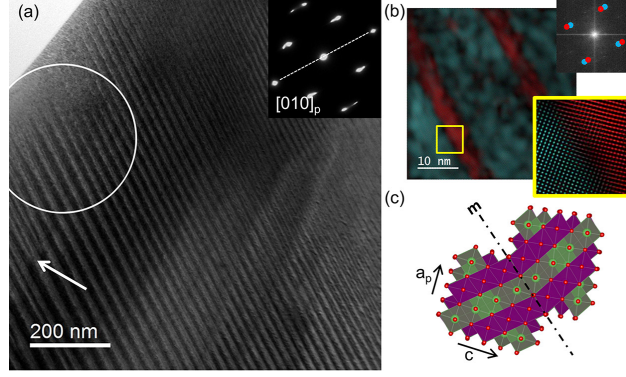


Figure 1: Lamellar structure of  $\text{Li}_{2x}\text{Mn}_2\text{O}_4$  [1] (Reproduced with permission from American Chemical Society).

## Theory

We propose a multi-scale thermomechanical continuum phase field model to predict microstructural evolution. This model is specifically designed to account for the interplay between diffusion and structural transformation and is adaptable for use with single crystal  $\text{Li}_{2x}\text{Mn}_2\text{O}_4$ .

### Free-energy functional

The crystal occupies a reference configuration  $\Omega$  with boundary  $\partial\Omega$ . Let  $\mathbf{x}$  be the position of a point on  $\Omega$  in this reference configuration. We are interested in the normalized chemical composition field  $\bar{c}(\mathbf{x}, t)$  and the mechanical displacement field  $\mathbf{u}(\mathbf{x}, t)$  in  $\Omega$ . The total free energy,  $\Psi(\bar{c}, \mathbf{u})$ , is the integral of the free energy density over the solid with boundary contributions included.

$$\begin{aligned}\Psi[\bar{c}, \mathbf{u}] &= \int_{\Omega} \hat{\psi}_{\text{bulk}}(\mathbf{F}, \bar{c}) + \hat{\psi}_{\text{grad}}(\nabla \mathbf{F}, \nabla \bar{c}) \, dV - \int_{\partial\Omega\{\boldsymbol{\tau}\}} \mathbf{u} \cdot \mathbf{T} \, dA \\ &= \int_{\Omega} \hat{\psi}_{\text{ther}}(\bar{c}) + \hat{\psi}_{\text{elas}}(\mathbf{F}) + \hat{\psi}_{\text{coup}}(\mathbf{F}, \bar{c}) + \hat{\psi}_{\text{grad}}(\nabla \mathbf{F}, \nabla \bar{c}) \, dV - \int_{\partial\Omega\{\boldsymbol{\tau}\}} \mathbf{u} \cdot \mathbf{T} \, dA\end{aligned}\quad (1)$$

Where  $\hat{\psi}_{\text{ther}}(\bar{c})$ ,  $\hat{\psi}_{\text{elas}}(\mathbf{F})$ , and  $\hat{\psi}_{\text{coup}}(\mathbf{F}, \bar{c})$  are the thermodynamic, elastic, and chemo-mechanically coupled free energy densities that are functions of normalized chemical composition,  $\bar{c}$ , deformation gradient,  $\mathbf{F}$ , at each fixed point  $\mathbf{x} \in \Omega$ . The gradient energy term  $\hat{\psi}_{\text{grad}}(\nabla \mathbf{F}, \nabla \bar{c})$  as a function of chemical composition gradient,  $\nabla \bar{c}$ , and gradient of deformation gradient,  $\nabla \mathbf{F}$ , penalizes changes in concentration and/or deformation gradient. Here  $F_{i,j} = \delta_{i,j} + u_{i,j}$  are the components of the deformation gradient tensor.

Assuming that the free energy densities are isotropic functions of their arguments [2] and satisfy both frame-indifference and material-symmetry [3], we can explicitly define these free-energy densities as follows:

$$\begin{aligned}\psi_{\text{ther}}(\bar{c}) &= RT_0 c_0 \left( [\bar{c} \ln \bar{c} + (1 - \bar{c}) \ln (1 - \bar{c})] + \mu_0 \bar{c} + \bar{c}(1 - \bar{c}) \sum_{i=1}^n \alpha_i (1 - 2\bar{c})^{i-1} \right) \\ \psi_{\text{elas}}(\mathbf{e}) + \psi_{\text{coup}}(\mathbf{e}, \bar{c}) &= \beta_1(\bar{c}) e_2^2 + \beta_3 e_2^4 + K(e_1 - \Delta V e_2^2)^2 + G e_6^2 \\ \psi_{\text{grad}}(\nabla \bar{c}, \nabla e_2) &= \frac{RT_0 c_0}{2} (\nabla \bar{c} \cdot \lambda \nabla \bar{c} + \nabla e_2 \cdot \kappa \nabla e_2)\end{aligned}\quad (2)$$

Where  $R$  and  $T_0$  represent the gas constant and temperature, respectively. The parameters  $\mu_0$  and  $\alpha_i$  are determined by fitting the open-circuit voltage (OCV) curve with a Redlich-Kister equation. Additionally, the bulk modulus  $K$  and shear modulus  $G$  are computed as  $K = \frac{C_{11}+C_{12}}{2}$  and  $G = C_{44}$  to reproduce the elastic constants ( $C_{11} = C_{1111}$ ,  $C_{12} = C_{1122}$ , and  $C_{44} = C_{1212}$ ) of the cubic phase. The coefficient  $\beta_1(\bar{c})$  characterizes the concentration-dependent deviatoric modulus governing the cubic to tetragonal transformations.  $\Delta V$  is lattice volume changes from lattice geometry measurements. Finally,  $e_1$ ,  $e_2$ , and  $e_6$  are re-parameterized symmetry-adapted strains:

$$e_1 = \frac{1}{\sqrt{2}}(E_{11} + E_{22}) \quad (3)$$

$$e_2 = \frac{1}{\sqrt{2}}(E_{11} - E_{22}) \quad (4)$$

$$e_6 = \sqrt{2}E_{12} \quad (5)$$

Where  $E_{IJ} = \frac{1}{2}(F_{kI}F_{kJ} - \delta_{IJ})$  are the components of the Green-Lagrange strain tensor.  $e_1$  introduces a compression or expansion of the square phase without symmetry change.  $e_2$  breaks the  $90^\circ$  rotational invariance of the square phase and a rectangular phase is obtained.  $e_6$  can introduce shear on the square phase. Doing so guarantees two order parameters  $\bar{c}$  and  $e_2$  to describe diffusion and structural transformation.

## Chemical equilibrium/non-equilibrium

In this subsection, we present the equations for non-equilibrium chemistry. By minimizing the free energy with respect to the concentration, we derive the chemical potential as shown in Eq. (6). This form of the chemical potential is equivalent to the one obtained through a microforce balance and the use of thermodynamically consistent constitutive relations, as discussed in [3].

$$\mu = \underbrace{\frac{1}{c_0} \frac{\partial \psi_{\text{ther}}}{\partial \bar{c}}}_{\mu_{\text{ther}}} + \underbrace{\frac{1}{c_0} \frac{\psi_{\text{elas}} + \psi_{\text{coup}}}{\partial \bar{c}}}_{\mu_{\text{coup}}} - \underbrace{RT_0(\nabla \cdot \lambda \nabla \bar{c})}_{\mu_{\text{grad}}} \quad (6)$$

Where  $\mu_{\text{ther}}$  is known as the homogeneous chemical potential.  $\mu_{\text{coup}}$  emerges due to the coupling between diffusion and mechanical deformation. Furthermore,  $\mu_{\text{grad}}$  comprises two terms: one results from the  $\nabla c$ , and the other arises from the coupling between  $\nabla e_2$  and  $\nabla c$ .

With the expression for the chemical potential Eq. (6) in hand, one can formulate the non-equilibrium chemistry problem using the mass balance law in conjunction with the phenomenological representation of the flux  $\mathbf{j}$ , that is:

$$\frac{\partial c}{\partial t} + \nabla \cdot \mathbf{j} = 0 \quad (7)$$

$$\mathbf{j} = -\mathbf{M}(c)\nabla \mu \quad (8)$$

Eq. (8) requires another boundary condition for  $j_n = \mathbf{j} \cdot \hat{\mathbf{n}}$  on  $\partial\Omega$ . Throughout this work, we choose a spatially independent mass flux at the surface as

$$j_n = \frac{\mathcal{C}c_0L}{3600 \cdot 3} \quad (9)$$

## Mechanical equilibrium

We assume that mechanical relaxation occurs significantly faster than ion transport and insertion, resulting in the system being in mechanical equilibrium while being chemically out of equilibrium. The mechanical governing equations for the system can be obtained through the minimization of the free energy with respect to the displacements or through thermodynamically consistent theory, yielding:

$$T_{R_{iJ,J}} - Y_{iJK,JK} = 0 \quad (10)$$

Where  $T_{R_{iJ}}$  are the components of the first Piola-Kirchhoff stress tensor and  $Y_{iJK}$  are the components of the higher-order stress tensor that are defined as:

$$T_{R_{iJ}} = \frac{\partial(\psi_e + \psi_{gd})}{\partial e_\alpha} \frac{\partial e_\alpha}{\partial F_{iJ}} + \frac{\partial \psi_{gd}}{\partial e_{\alpha,m}} \frac{\partial e_{\alpha,m}}{\partial F_{iJ}} \quad (11)$$

$$Y_{iJK} = \frac{\partial \psi_{gd}}{\partial e_{\alpha,m}} \frac{\partial e_{\alpha,m}}{\partial F_{iJ,K}} \quad (12)$$

The weak form for mechanical equilibrium Eq. (10) will be solved in conjunction with the weak form for the non-equilibrium chemistry problem.

## Results

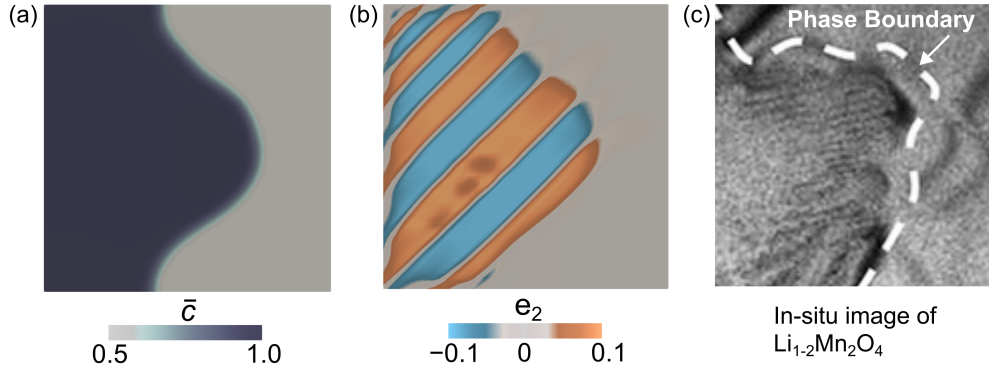


Figure 2: We compare microstructural features predicted in our simulation with the experimental image of  $\text{Li}_{2x}\text{Mn}_2\text{O}_4$ . (a-b) The Li-composition and strain variant distribution at SOC = 78.52% shows a curved phase boundary and finely twinned microstructures. This prediction compares favorably with the bright field imaging  $\text{Li}_{2x}\text{Mn}_2\text{O}_4$  by [1](Reproduced with permission from American Chemical Society).

We compare our modeling predictions with previously published in-situ bright field imaging of microstructural patterns in  $\text{Li}_{2x}\text{Mn}_2\text{O}_4$  [1], see Fig. 2. We note similarities between our simulations and the experimental images: First, the phase boundary separating the  $\text{Li}_2\text{Mn}_2\text{O}_4/\text{LiMn}_2\text{O}_4$  phases is curved in both our simulation and the experimentally imaged microstructure. This curved morphology does not correspond to the energy-minimizing orientation of the phase boundary in equilibrium and arises from the dynamic boundary conditions applied on the electrode surface. Second, as observed in experiments, the tetragonal lattice variants nucleate independently in our computations and evolve to form compatible twin interfaces. Overall, the similarities between experiments and theoretical predictions show that our modeling framework captures the

interplay between Li-diffusion and lattice deformations, and this model could in turn be used as a tool to crystallographically design microstructures in intercalation compounds.

## References

1. Erichsen, T., Pfeiffer, B., Roddatis, V. & Volkert, C. A. Tracking the diffusion-controlled lithiation reaction of  $\text{LiMn}_2\text{O}_4$  by In Situ TEM. *ACS Appl. Energy Mater.* **3**, 5405–5414 (2020).
2. Anand, L. A Cahn–Hilliard-type theory for species diffusion coupled with large elastic–plastic deformations. *Journal of the Mechanics and Physics of Solids* **60**, 1983–2002 (2012).
3. Zhang, T., Zhang, D. & Balakrishna, A. R. Coupling Diffusion and Finite Deformation in Phase Transformation Materials. *arXiv preprint arXiv:2309.01870* (2023).